

AEROELASTIC CFD COMPUTATIONS FOR ROTOR FLOWS

Florent Dehaeze and George N. Barakos

CFD Laboratory, Department of Engineering
University of Liverpool, L69 3GH, U.K.

<http://www.liv.ac.uk/flightscience/PROJECTS/CFD/ROTORCRAFT/RBD/index.htm>

Email: Florent.Dehaeze@liverpool.ac.uk, G.Barakos@liverpool.ac.uk

Abstract

The use of aeroelastic coupling for rotorcraft simulations improves flow field predictions, therefore rotorcraft CFD codes should allow for this type of analysis. This paper presents a coupling method able to perform quick mesh deformations and aeroelastic predictions for both hovering and forward flying rotors. This method takes into account the specifics of the HMB solver. A coupling method is first demonstrated for hovering rotors using the UH-60A rotor as an example. The HART-II rotor in forward flight is then used to demonstrate deformation during a flight, using a prescribed shape from experimental measurements. The mesh demonstration method proved to be efficient with very low CPU and RAM overhead.

NOMENCLATURE

		Re	Reynolds number
		S	Vorticity magnitude
		SALSA	Strain Adaptative Linear Spalart-Allmaras model
		SA	Spalart-Allmaras model
		St	Strouhal number
		U_∞	Freestream velocity
		URANS	Unsteady Reynolds Average Navier-Stokes
		C_T	Rotor thrust coefficient
		α_S	Shaft angle of the rotor, positive backward
		β_0	Coning angle of the rotor
		β_{1c}, β_{1s}	Cyclical flapping angle of the rotor
		χ	Ratio of the undamped viscosity and the molecular viscosity $\chi = \tilde{\nu}/\nu$
		ΔU	Difference between the velocity at the field point
		Δx	Grid spacing along the wall at the trip
		Δ	Mesh length scale
		δ	Boundary layer thickness
		$\Delta_x, \Delta_y, \Delta_z$	Mesh length scale
		κ	Kármán constant
		μ	Forward flight advance ratio
		ν	Molecular viscosity
		ν_t	Kinematic eddy viscosity
		ω_t	Wall vorticity at the trip
		σ	Turbulent Prandtl number
		θ_0	Collective angle of the rotor
		θ_{1c}, θ_{1s}	Cyclical pitch angle of the rotor
		$\tilde{\nu}$	Undamped eddy viscosity
c	Chord length		
C_{b1}	Production correction factor in the SALSA model		
$c_{b1}, c_{b2}, c_{w1}, c_{w3}, c_{t3}, c_{t4}$	SA turbulence model constants		
C_{DES}	Mesh length scale scaling in the DES and DDES models		
\tilde{d}	DES and DDES models length scale		
d	Wall-distance		
DES	Delayed Detached-Eddy Simulation		
DDES SALSA	Delayed Detached-Eddy Simulation with the SALSA production term modification		
DES	Detached-Eddy Simulation		
DES SALSA	Detached-Eddy Simulation with the SALSA production term modification		
d_t	Distance from the field point to the trip		
f_d	B function in the DDES model		
$f_{t1}, f_{t2}, f_{v2}, f_{v1}, f_w$	SA turbulence model empirical functions		
l_{RANS}	RANS model length scale		
M	Mach number		
M_∞	Freestream Mach number		
$M^2 C_n$	Mach scaled normal coefficient		
$P_{\tilde{\nu}_t}$	Production term in the SALSA model		
R	Rotor radius		
RANS	Reynolds Averaged Navier-Stokes		
r_d	Root of the ratio between the length scale and the wall distance		

1 INTRODUCTION

Rotorcraft calculations are still challenging, mainly due to interactions between the wake and the rotor. This has a strong influence on the blade loads and structural deformations. Therefore, improvement to the flow predictions can be achieved by coupling the rotor aerodynamics with the structural deformation, as well as selecting an accurate flow field model able to capture the properties of the flow-field.

Aeroelastic coupling is a popular research subject within the last years and many studies aimed at predicting the blade structural deformations as well as the flow field. Two main coupling strategies are available: the weak coupling and the strong one [2].

Weak coupling is currently the most popular method. With this method, the ONERA 7A and 7AD rotors were studied by Pahlke *et al.* [15] at high advance ratio ($\mu = 0.4$) using the FLOWer RANS solver coupled with the S4 structural solver. The comparison of the torsional deformation at the tip shows that while the amplitude is equivalent, the 5/rev content was not captured for both rotors. The UH-60A rotor in various forward flight conditions was studied by Potsdam *et al.* [22] with coupled OVERFLOW-CAMRAD methods. The use of CFD was also assessed against a lifting line model by Datta *et al.* [7] who used TURNS (CFD) and UMARC (Lifting line model) for the UH-60A in forward flight. The use of CFD improved the torsional predictions particularly on the advancing side and the higher harmonics of the flapping bending moment. Another popular test case is the HART-II rotor. Lim *et al.* [17] coupled CAMRAD and OVERFLOW and captured the blade-vortex interactions (BVI). However, the amplitude of the oscillations of the Mach-scaled normal force coefficient tends to be under-predicted. Their grid convergence study highlights the need for a fine grid to capture the BVI. Jung *et al.* [14] used the same case to test a loose coupling procedure between CAMRAD or DYMORE and KFLOW. The BVIs were accurately captured. However, the flapping amplitude on the advancing side was under-predicted and the lead-lag tip displacement was offset. A weak coupling strategy was also employed by Biedron *et al.* [5] along with FUN3D and CAMRAD II. A prescribed motion simulation using experimental deformation measurements and a coupled simulation were compared. Despite the smaller torsional deformation amplitudes at the tip in the coupled simulations, the normal force coefficient predictions at $r/R = 0.87$ proved similar, with just small differences in the first quarter of the rotor revolution.

The strong coupling method was tested by Pomin *et al.* [12] for the ONERA 7A rotor at high advance ratio ($\mu = 0.4$). While the results agree fairly well with experimental measurements, the down peak on the advancing side was under-predicted. A comparison of strong and weak coupling methods was also carried out by Altmikus *et al.* [2]. The differences between the strong and the weak coupling results proved limited, however the weak coupling method proved more robust. An advantage of the strong coupling method comes in allowing manoeuvring flights simulations to be performed. This was demonstrated by Sitaraman *et al.* [26] who simulated a pull-up manoeuvre for the UH-60A.

Aeroelastic computations of hovering rotors proved less popular. Beaumier *et al.* [4] coupled the FLOWer and CA-

NARI RANS solver with structural deformations obtained from Eurocopter R85 code for hovering ONERA 7A and Bo-105 rotors. The influence at a given thrust on the figure of merit proved limited however a higher collective was needed to reach the same thrust on the elastic blade to compensate the torsional deformation, which reached -0.5 degree on the ONERA 7A rotor and -2 degrees on the Bo-105 rotor. The magnitude of the predicted ONERA 7A blade deformation in hover was similar in the simulation from Pomin *et al.* [12] when coupling INROT and DYNROT.

This paper discusses the coupling method used with the Helicopter Multi-Block (HMB) solver using the NASTRAN structural solver. Two coupling methods have been developed. The first method takes advantage of the steadiness of a hovering rotor, while the second describes a strong coupling method for a forward flying method using a strong coupling, which allows more flexibility in the flight definition.

In the next section, the numerical methods are described, including the aeroelastic coupling procedure. This is followed by CFD simulations. The first simulation deals with a hovering UH-60A rotor. The HART-II rotor in forward flight is then used to demonstrate the potential of DES simulations with a prescribed deformation from experimental measurements.

2 NUMERICAL METHODS

2.1 Aerodynamic Modelling

2.1.1 Helicopter Multi-Block solver

The Helicopter Multi-Block(HMB) code, developed in Liverpool, is used as the CFD solver for the present work. It solves the Navier-Stokes equations in integral form using the arbitrary Lagrangian Eulerian (ALE) formulation for time-dependent domains with moving boundaries:

$$\frac{d}{dt} \int_{V(t)} \vec{w} dV + \int_{\partial V(t)} \left(\vec{F}_i(\vec{w}) - \vec{F}_v(\vec{w}) \right) \vec{n} dS = \vec{S} \quad (1)$$

where $V(t)$ is the time dependent control volume, $\partial V(t)$ its boundary, \vec{w} is the vector of conserved variables $[\rho, \rho u, \rho v, \rho w, \rho E]^T$. \vec{F}_i and \vec{F}_v are the inviscid and viscous fluxes, including the effects of the time dependent domain. For hovering rotor simulations, the grid is fixed and a source term $\vec{S} = [0, -\rho \vec{\omega} \times \vec{u}_h, 0]^T$ is added to compensate for the inertial effects of the rotation. \vec{u}_h is the local velocity field in the rotor-fixed frame of reference.

The Navier-Stokes equation are discretised using a cell-centred finite volume approach on a multi-block grid, leading to the following equations:

$$\frac{\partial}{\partial t} (\mathbf{w}_{i,j,k} V_{i,j,k}) = -\mathbf{R}_{i,j,k}(\mathbf{w}_{i,j,k}) \quad (2)$$

where \mathbf{w} represents the cell variables and \mathbf{R} the residuals. i, j and k are the cell indices and $V_{i,j,k}$ is the cell volume. Osher's [21] upwind scheme is used to discretise the convective terms and MUSCL variable interpolation is used to provide third order accuracy. Van Albada limiter is used to reduce the oscillations near steep gradients.

Temporal integration is performed using an implicit dual-time step method. The linearised system is solved using the

generalised conjugate gradient method with a block incomplete lower-upper (BILU) pre-conditioner [3].

Multi-block structured meshes are used for HMB. These meshes are generated using ICEM-Hexa™ of Ansys. The multi-block topology allows for an easy sharing of the calculation load for parallel computing. For rotor flows, a typical multi-block topology used in the University of Liverpool is described in [23]. A C-mesh is used around the blade and this is included in a larger H structure which fills up the rest of the computational domain. The block boundaries on a hover flying straight blade rotor is shown in black in Fig. 1. Rotor trimming, corresponding to rigid movements of the blade, is obtained by a rigid motion of the whole C-Part of the mesh, shown in grey in Fig. 1. This preserves the mesh quality around the blade surface. The layer of blocks around the C-part is then re-meshed using Trans-Finite Interpolation method [9].

2.1.2 Turbulence Models for Flow Simulations

The most popular turbulence models in the rotorcraft community are based on the 2-equations $k-\omega$ turbulence model. The Spalart-Allmaras (SA) 1-equation turbulence model is also gaining popularity. However, these turbulence models have limitations on the range of low scales that can be predicted and the higher frequencies are only modelled. These limitations can be overcome by using the DES model, based on the SA model. These turbulence models are described in this section.

Spalart-Allmaras Model The one-equation Spalart-Allmaras (SA) turbulence model [28] solves a transport equation for the eddy viscosity directly. The kinematic eddy viscosity, (ν_t), in the SA model is calculated by

$$\nu_t = \tilde{\nu} \cdot f_{v1} \quad , \quad (3)$$

where

$$f_{v1} = \frac{\chi^3}{\chi^3 + c_{v1}^3} \quad \text{and} \quad \chi = \frac{\tilde{\nu}}{\nu} \quad .$$

In the above equations, and hereafter, the term f refers to a function, c refers to a constant, ν is the molecular viscosity and $\tilde{\nu}$ is the undamped eddy viscosity that obeys the following transport equation:

$$\begin{aligned} \frac{D\tilde{\nu}}{Dt} &= c_{b1} (1 - f_{t2}) \tilde{S} \tilde{\nu} \\ &+ \frac{1}{\sigma} \left(\nabla \cdot ((\nu + \tilde{\nu}) \nabla \tilde{\nu}) + c_{b2} (\nabla \tilde{\nu})^2 \right) \\ &- \left(c_{w1} f_w - \frac{c_{b1}}{\kappa^2} f_{t2} \right) \left(\frac{\tilde{\nu}}{d} \right)^2 + f_{t1} \Delta U^2 \quad . \end{aligned} \quad (4)$$

The first term on the right-hand side is the production term, the second is the diffusion term and the third is the near-wall term. The last term models transition downstream of tripping. The subscript b stands for *basic*, w for *wall* and t for *trip*. The parameter σ represents the turbulent Prandtl number and d is the wall-distance.

The term \tilde{S} in Equation (4) is defined by the following equation, where S is the vorticity magnitude:

$$\tilde{S} = S + \frac{\tilde{\nu}}{\kappa^2 d^2} f_{v2} \quad , \quad (5)$$

$$f_{v2} = 1 - \frac{\chi}{1 + \chi f_{v1}} \quad . \quad (6)$$

The function f_w in Equation (4) is given by:

$$f_w = g \left(\frac{1 + c_{w3}^6}{g^6 + c_{w3}^6} \right)^{1/6} \quad , \quad (7)$$

$$g = r + c_{w2} (r^6 - r) \quad , \quad (8)$$

$$r = \frac{\tilde{\nu}}{\tilde{S} \kappa^2 d^2} \quad (9)$$

The f_{t2} function is defined by:

$$f_{t2} = c_{t3} \cdot e^{-c_{t4} \chi^2} \quad . \quad (10)$$

The trip function f_{t1} is defined as

$$f_{t1} = c_{t1} g_t \cdot e^{-c_{t2} \frac{\omega_t^2}{\Delta U^2} (d^2 + g_t^2 d_t^2)} \quad , \quad (11)$$

where d_t is the distance from the field point to the trip, ω_t is the wall vorticity at the trip, ΔU is the difference between the velocity at the field point and that at the trip and $g_t = \min(0.1, \Delta U / \omega_t \Delta x)$, in which Δx is the grid spacing along the wall at the trip.

Values used for the SA turbulence model constants are given in Tab. 1. The constant c_{w1} is defined as

$$c_{w1} = \frac{c_{b1}}{\kappa^2} + \frac{(1 + c_{b2})}{\sigma} = 3.2391 \quad . \quad (12)$$

A value of $2/3$ has been used for the turbulent Prandtl number, σ .

Detached-Eddy Simulation (DES) Despite its potential, the need of fine grids close to the wall does not allow the use of Large-Eddy Simulation (LES) in complex flows. Detached-Eddy Simulation may be an alternate. The main principle of these models is the use of RANS close to the walls and LES further.

The original idea of DES was postulated by Spalart *et al.* [27]. The RANS equations with a modified length scale are used in the whole domain, though the length scale is also depending on the mesh size. In the RANS areas, the usual RANS length scale will be used, but in the LES zones, the length scale will now depend on the mesh length scale, forcing the turbulence model to behave like LES. DES does not need an interface between the RANS and LES part.

Spalart introduced the mesh length scale Δ as a function of the cell size following the three axis Δ_x , Δ_y and Δ_z :

$$\Delta = \max(\Delta_x, \Delta_y, \Delta_z) \quad . \quad (13)$$

The new length scale for DES is then:

$$l_{DES} = \min(l_{RANS}, C_{DES} \Delta) \quad , \quad (14)$$

where C_{DES} is an arbitrary constant. For example, in the case of the SA model, the scale length l_{RANS} is the wall distance d . In the new DES model, the length scale \tilde{d} is defined as:

$$\tilde{d} = \min(d, C_{DES} \Delta) \quad . \quad (15)$$

Therefore, near walls, the model will use the RANS equations, and further away, the length scale will switch to the grid length scale and the model will behave like LES.

This modification aims at increasing the dissipation term of the turbulent kinetic energy and thus decrease the production term. The dissipation term is now equal to:

$$-C_{w1}f_{w1}\left(\frac{\tilde{v}}{\tilde{d}}\right)^2. \quad (16)$$

2.2 Structural Modelling

NASTRAN is used to calculate the static structural deformations and perform modal analysis of the structural model. The blade is represented using a beam model. Non-linear CBEAM elements are used along the quarter-chord line in the blade and contain all the blade structural properties. A non-linear static analysis was performed (SOL 106), taking into account the rotational inertia. An iterative process allowed for the large displacements to be taken into account while recomputing the forces due to the aerodynamic loads and the centrifugal forces at each step. The main properties needed for this analysis are the distribution of the sectional area, the chordwise and flapwise area moments of inertia, the torsional constant and the linear mass distribution along the span. Other data like the offset between the elastic axis and the centre of gravity along the span can be added to refine the analysis. All the structural properties are linearly interpolated between both ends of the beam element. CBAR elements without any structural properties are used to interpolate the beam model deformation to the blade surface, which is used to deform the fluid grid.

The UH-60A blade [1] and HART-II blade [31] are used as examples to describe the models developed in NASTRAN. The UH-60A blade geometry has a rectangular plan shape until $r/R = 0.93$ from where the tip is swept back at 20degrees. Two aerofoil sections are used, with linear transitions in between: the SC1095 from $r/R = 0.1925$ to $r/R = 0.4658$ and from $r/R = 0.8540$ to the tip, and the SC1094R8 from $r/R = 0.4969$ to $r/R = 0.8230$. The blade has non-linear twist as reported in [1]. The NASTRAN model contains 89 CBEAM elements along the blade span. The UH-60A blade properties were reported by Hamade *et al.* [13]. The blade model is attached to the hub at station $r/R = 0.093$ and is not allowed any translation at the root. The blade is free to rotate in flapping and lead-lag but the root of the blade is not allowed to have any torsional deformation. A lead-lag damper and a flapping spring were added as elastic elements with a strength of 353lbf.ft/rad. A dynamic validation of the UH-60A is presented in Fig. 2.

The HART-II blade has a rectangular planform. A NACA23012 aerofoil with a 5mm tab is used along the blade span. The twist is linear at -8degrees/R. The structural model contains 42 elements along the blade span.

2.2.1 Grid Deformation Method

The method developed for HMB first deforms the blade surface using the Constant Volume Tetrahedron (CVT) method, then obtains the updated block vertex positions via spring

analogy (SAM) and finally generates the full mesh via Transfinite Interpolation (TFI). The TFI first interpolates the block edges and faces from the new vertex position and then interpolates the full mesh from the surfaces. This method uses the properties of multi-block meshes and maintains efficiency as the number of blocks increases, particularly in the spanwise blade direction. This approach is not reported elsewhere in the literature since most authors deform the complete mesh using the mode shapes. The proposed method provides more flexibility and allows for complex multi-block topologies to be used. In addition it gives more control over the distribution of mesh deformation in the computational domain.

Constant Volume Tetrahedron (CVT) Method The Constant Volume Tetrahedron (CVT) method developed by Goura [10] allows quick deformation calculations. This method projects each fluid node to the nearest structural triangular element and moves it linearly with the element.

Each node of the blade surface (F) is associated to the nearest structural element (S_1, S_2, S_3) as shown in Fig. 4a and projected as follows:

$$\vec{c} = \alpha\vec{a} + \beta\vec{b} + \gamma\vec{d} \quad (17)$$

where $\vec{a} = \overrightarrow{S_1S_2}$, $\vec{b} = \overrightarrow{S_1S_3}$, $\vec{c} = \overrightarrow{S_1F}$ and $\vec{d} = \vec{a} \wedge \vec{b}$. The coefficients α , β and γ can then be expressed as:

$$\alpha = \frac{(\vec{a} \cdot \vec{c}) \|\vec{b}\|^2 - (\vec{a} \cdot \vec{b}) (\vec{b} \cdot \vec{c})}{\|\vec{a}\|^2 \|\vec{b}\|^2 - (\vec{a} \cdot \vec{b})^2} \quad (18)$$

$$\beta = \frac{(\vec{b} \cdot \vec{c}) \|\vec{a}\|^2 - (\vec{a} \cdot \vec{b}) (\vec{a} \cdot \vec{c})}{\|\vec{a}\|^2 \|\vec{b}\|^2 - (\vec{a} \cdot \vec{b})^2} \quad (19)$$

$$\gamma = \frac{(\vec{c} \cdot \vec{d})}{\|\vec{a}\|^2 \|\vec{b}\|^2 - (\vec{a} \cdot \vec{b})^2}. \quad (20)$$

The new position of the deformed blade fluid point is obtained by calculating:

$$\vec{c}' = \alpha\vec{a}' + \beta\vec{b}' + \gamma\vec{d}', \quad (21)$$

where \vec{a}' , \vec{b}' , \vec{c}' and \vec{d}' are the same vectors after the structural deformation.

CVT is an efficient deformation method, however, it showed limitations when getting further from the blade. The linear association with the triangular structural elements can create discrepancies between two close nodes associated with two different structural elements as shown in Fig. 3. Therefore the mesh deformation further from the blade surface has to be performed with a different method. A transfinite interpolation (TFI) of the mesh was therefore introduced in the C-part of the mesh.

Trans-Finite Interpolation (TFI) The Trans-Finite Interpolation (TFI), described by Dubuc *et al.* [9], is used to interpolate the block face deformation from the edge deformations and then the full block deformation from the deformation of the block faces.

The mesh deformation uses a weighted approach to interpolate a face/block from the boundary vertices/surfaces respectively. The weight depends on the curvilinear coordinate divided by the length of the curve. The notation used here is shown in Fig. 4b. The generation of the mesh on a block face ($\vec{x}_1, \vec{x}_2, \vec{x}_3, \vec{x}_4$) can be expressed as:

$$\begin{aligned} d\vec{x}(\xi, \eta) &= \vec{f}_1(\xi, \eta) \\ &+ \phi_1^0(\eta)[d\vec{x}_1(\xi) - \vec{f}_1(\xi, 0)] \\ &+ \phi_2^0(\eta)[d\vec{x}_3(\xi) - \vec{f}_1(\xi, 1)], \end{aligned} \quad (22)$$

where \vec{f}_1 is defined as:

$$\vec{f}_1(\xi, \eta) = \psi_1^0(\xi)d\vec{x}_4(\eta) + \psi_2^0(\xi)d\vec{x}_2(\eta), \quad (23)$$

with $d\vec{x}_1, d\vec{x}_2, d\vec{x}_3$ and $d\vec{x}_4$ representing the displacements of the four faces corners and ϕ and ψ representing the blending functions in the η and ξ directions. The blending functions are expressed as a function of the stretching functions s_1, s_2, s_3 and s_4 :

$$\psi_1^0(\eta) = 1 - s_1(\xi) \quad (24)$$

$$\psi_2^0(\eta) = s_3(\xi) \quad (25)$$

$$\phi_1^0(\eta) = 1 - s_4(\eta) \quad (26)$$

$$\phi_2^0(\eta) = s_2(\eta). \quad (27)$$

The stretching function s_1 is defined by:

$$s_1(\xi) = \frac{\widehat{x_1x_2}(\xi, 0)}{\widehat{x_1x_2}}, \quad (28)$$

where $\widehat{x_1x_2}$ is the curvilinear length between \vec{x}_1 and \vec{x}_2 . s_2, s_3 and s_4 are defined in a similar way for the curves x_2x_3, x_3x_4 and x_4x_1 respectively. The interpolation of the inside of the block from the shape of the block faces follows the same method.

This interpolation was introduced in the C-part of the mesh giving good results in terms of mesh quality but was limited in amplitude due to the small size of the C-part, as shown in Fig. 5. The block edges are not moved and therefore the maximum amplitude for each point has to be limited to a fraction of the C-part height, which often is about $0.2c$. However, this limit in the displacement of the blade surface can easily be exceeded for rotor cases. To overcome this limit, the boundaries of the blocks around the blades also have to be moved according to the blade deformation, and damping must be introduced when getting further from the blade to get no deformation at the calculation boundaries. Particular attention must also be given to the mesh quality close to the blade as CFD calculations are sensitive to a loss of quality in the refined mesh parts close to the blade.

Spring Analogy (SAM) To overcome the problem demonstrated on Fig. 5, the spring analogy was used. The spring analogy [6] consists of adding springs on each block surface side and diagonal of the mesh. The springs along the sides of the surfaces tend to avoid large compression or dilatation of the block surfaces and the ones on the diagonals tend to limit skewness, which is critical in some parts of the mesh like the tip of the blade where the cells are usually skewed.

The strength of the springs is set as the inverse of their length and the springs in contact with the blade are usually made stiffer by a coefficient arbitrarily set to 50 in order to make the blocks close to the blade surface extremely rigid. An example of spring location and stiffness for a C-mesh around an airfoil is shown in Fig. 6, where the springs on two faces are shown with black and dark grey dashed lines. The black lines represent the normal springs inside the computational domain and the dark grey ones are in contact with the blade and are therefore made stiffer. The force on each vertex is calculated as the sum of the forces due to the neighbouring springs:

$$\vec{F}_i = \sum_{j=1}^{n_i} k_{ij} (\vec{\delta}_j - \vec{\delta}_i), \quad (29)$$

where n_i is the number of vertices connected to the i -th vertex, k_{ij} is the stiffness of the spring between the i -th and j -th nodes and $\vec{\delta}_i$ is the displacement vector of the i -th node.

The connection of the springs between the nodes instead of the nodes and their original position is justified by the large displacements being undergone by the blades and the need to keep the blocks close to the blade as close as possible to their undeformed shape.

The displacement of the nodes on the blade surface is forced and a new equilibrium is reached. The nodes on the blade and the far-field are fixed, and the new equilibrium position of the interior nodes is obtained by solving, for each node, the equation:

$$\sum_{j=1}^{n_i} \vec{F}_{ij} = \vec{0}, \quad (30)$$

where \vec{F}_{ij} is the force exerted on the i -th node by the spring between the i -th and j -th nodes and is defined by $\vec{F}_{ij} = k_{ij} (\vec{\delta}_j - \vec{\delta}_i)$. Equation 30 can then be written as:

$$\sum_{j=1}^{n_i} k_{ij} (\vec{\delta}_j - \vec{\delta}_i) = 0. \quad (31)$$

The above system of equations can also be written for each $\vec{\delta}_i$ as:

$$\vec{\delta}_i = \frac{\sum_{j=1}^{n_i} k_{ij} \vec{\delta}_j}{\sum_{j=1}^{n_i} k_{ij}} \quad (32)$$

and solved iteratively, by using the algorithm:

$$\vec{\delta}_{i,new} = \frac{\sum_{j=1}^{n_i} k_{ij} \vec{\delta}_{j,old}}{\sum_{j=1}^{n_i} k_{ij}}. \quad (33)$$

This iterative process is initialised with the undeformed location of the nodes except for the one on the blade surface which are set to the deformed position. It is repeated about 1,000 times, which was enough to reach convergence even on meshes with a large number (about 2000) of vertices. The convergence criterion employed here was:

$$error = \sqrt{\sum_{i=1}^{n_v} \|\vec{\delta}_{i,new} - \vec{\delta}_{i,old}\|^2}. \quad (34)$$

2.2.2 Rotor Trimmer

A simple grid trimmer for hovering rotors based the blade element theory described in [23] was used for this work. This model is mainly based on the lock number γ_L of the blade and computes an initial trim state for a hovering rotor. Firstly, the collective is estimated as:

$$\theta_0 = \frac{3}{\sigma a_l} C_T + \frac{3}{2} \sqrt{\frac{C_T}{4}} \quad , \quad (35)$$

where $C_T = \frac{T}{\frac{1}{2} \rho A (\Omega R)^2}$ is the thrust coefficient, a_l is the lift slope factor, assumed as 5.7, and $\sigma = \frac{N_b c}{\pi R}$ is the rotor solidity, with N_b the number of rotor blades. The inflow factor λ is then estimated by:

$$\lambda = -\sqrt{\frac{C_T}{4}} = -\frac{\sigma a}{16} \left[\sqrt{1 + \frac{64}{3\sigma a} \theta_0} - 1 \right] \quad , \quad (36)$$

and the coning β_0 is:

$$\beta_0 = \frac{\gamma}{8} \left[\theta_0 + \frac{4}{3} \lambda \right] \quad . \quad (37)$$

HMB is then used to compute the actual thrust coefficient $C_{T,CFD}$ at this particular trimming.

The next step uses the resulting thrust coefficient to update the trim state. The collective is updated with $\delta\theta_0$ defined as follows:

$$\delta\theta_0 = \frac{C_{T,Target} - C_{T,CFD}}{\frac{dC_T}{d\theta_0}} \quad , \quad (38)$$

with $\frac{dC_T}{d\theta_0}$ being obtained solving the following equation:

$$\frac{dC_T}{d\theta_0} = \frac{\sigma a}{6} \left[1 - \frac{1}{\sqrt{1 + \frac{64}{3\sigma a} \theta_0}} \right] \quad . \quad (39)$$

The coning is then obtained using Equation 37, and this step is repeated until convergence is reached.

2.3 Aeroelastic coupling method

Two aeroelastic coupling methods have been developed for HMB, based on the flight type. Hovering rotors can be modelled as steady calculations and therefore a static deformation can be obtained from NASTRAN to deform the blade. The loading is extracted from the CFD results by extracting the sectional loads at the structural nodes location. The new blade shape is then introduced in the fluid grid using the previously described mesh deformation method and the flow is updated. This steps are repeated until convergence on the loads is reached.

For forward flying rotors, this method is not applicable and therefore a modal approach is used. The eigenmodes are obtained in NASTRAN and then the blade shape is described as a linear combination of those:

$$\phi = \phi_0 + \sum_{i=1}^{n_m} \alpha_i \phi_i \quad , \quad (40)$$

where ϕ is the blade shape, ϕ_0 the blade static deformation and ϕ_i is the i -th mass-scaled eigenmode of the blade. The amplitude coefficients α_i are obtained by solving the equation:

$$\frac{\partial^2 \alpha_i}{\partial t^2} + 2\zeta_i \omega_i \frac{\partial \alpha_i}{\partial t} + \omega_i^2 \alpha_i = \vec{f} \phi_i \quad , \quad (41)$$

where ω_i and ζ_i are respectively the eigenpulsation and the eigenmode damping ratio. \vec{f} is the vector of external forces. A strong coupling approach was chosen, therefore the eigenmode amplitude coefficients were assessed at each time step by solving the following equation:

$$[\alpha_i]_{t+1} = [\alpha_i]_t + \left[\frac{\partial \alpha_i}{\partial t} \right]_t \Delta t + \frac{1}{2} \left[\frac{\partial^2 \alpha_i}{\partial t^2} \right]_t \Delta t^2 \quad , \quad (42)$$

where Δt is the time step.

3 RESULTS AND DISCUSSION

3.1 DES Evaluation

The DES models implementation was tested using a NACA0021 aerofoil at a high incidence of 60 degrees. A comparison with experimental measurements obtained by Swalwell *et al.* [29] was carried out in [8]. The flow was computed on a grid with 1.1 million nodes on a mesh covering 2 chord lengths of span. An O-topology was used. Symmetry boundary conditions were applied on both planes at the tips of the wing, and the far field was located at 15 chords. The trailing edge was sharpened for the calculation. The tested turbulence models were the standard Spalart-Allmaras (SA), the Detached-Eddy Simulation (DES) and the Delayed Detached-Eddy Simulation (DDES). These models were also tested with the SALSA production term modification developed by Rung *et al.* [24]. Finally, an assessment of the effect of the filtering C_{DES} coefficient was carried out by repeating the same calculation with a halved C_{DES} coefficient. The grid supplied by the NTS¹ was also tested as well as a double sized version of the coarse grid.

A $2c$ span size was chosen following the length advised by Guenot [11]. Guenot's study was performed for an incidence of 45 degrees and DESider members found this length the be underestimated, probably because of the change in incidence. A length of $2.8c$ would be more adapted.

The FFT of the lift and drag coefficients were computed and compared to the experimental measurements obtained by Swalwell *et al.* [29] in Fig. 7. The main difference between URANS and DES predictions lies in the nature of the flow: while the former ones predicted a steady flow, the latter ones predicted a fully unsteady flow with a vortex shedding in the wake of the aerofoil. This is visible in the lift and drag coefficients in FFT with the URANS models having very low amplitudes compared to the ones obtained through DES. The DES results showed two peaks corresponding to the shedding of the vortices in the wake. The comparison of the experimental measurements with the DES models predictions was good, with the peaks located at the same frequencies. The main difference appears in the higher frequencies where the slope is over-predicted by the DES models.

¹New Technologies and Services

3.2 UH-60A Rotor in Hover Flight

The UH-60A rotor is used to demonstrate and assess the aeroelastic coupling method for hovering rotors. Wind-tunnel measurements were obtained by Lorber *et al.* [18, 19] for a thrust coefficient of $C_T/\sigma = 0.170$ on a model rotor. This corresponds to $C_T = 0.01404$. The UH-60A rotor was Mach-scaled with a diameter 5.73 times smaller than the real rotor and some deformation was included in the blade to reflect the deformations undergone by the blade in flight. The exact geometry of the model blade along with its structural properties were not available, and more particularly uncertainties exist about the blade twist. Therefore, it was decided to compare the experimental results with a numerical simulation of the full scale rotor at the same thrust coefficient. The flight conditions then become: tip Mach number of $M_{tip} = 0.63$, Reynolds number based on the tip speed and chord length $Re_{tip} = 7.833 \times 10^6$. It was also decided to use the assessed experimental Reynolds number $Re_{tip} = 1.367 \times 10^6$ for comparison, since the viscosity would have more effect on the torque. The experimental results contain integrated values including the thrust and torque moments and figure of merit, pressure taps along the blade span at 8 radial stations and the vortices position in the wake. The pressure taps are located at $r/T = 0.4, 0.55, 0.675, 0.775, 0.865, 0.92, 0.945$ and 0.965 .

The first calculation was done for an inviscid flow with a small grid (1.5 million nodes), while the following ones were on a bigger grid (9 million nodes) with a viscous flow model and the $k - \omega$ BSL turbulence model of Menter [20]. The viscous calculation was first run for a rigid blade at each Reynolds number, and then structural deformations were introduced. Each calculation was trimmed to the experimental thrust coefficient, using the grid trimmer presented previously. To obtain the coning angle from the trimmer, a lock number of 8 was used for both the full-scale and model blades, as used by Kim [16]. The structural model used corresponds to the real blade, due to the lack of properties for the model rotor. An example of rotor trimming is presented in Fig. 8, where the trimming of the rigid and elastic (third aeroelastic coupling iteration) UH-60A blades with viscous flow model is presented. A converged trim state was obtained after seven iterations for the rigid case and three for the elastic case, due to a better assessment of the initial collective angle thanks to the previous elastic iterations.

The structural deformations were recomputed after each CFD simulations, and the convergence of the blade loads was quick: three elastic iterations allowed to get converged loads. The main differences between the inviscid simulation and the viscous ones are near the tip area, between $r/R = 0.70$ and $r/R = 1$. This is mainly due to the coarseness of the inviscid grid compared to the viscous ones: the flow features in the area near the sweep back were not well captured in the inviscid case. The vertical loading of the elastic blade is slightly stronger in the main part of the blade than the loading of the rigid blade, while it is lower closer to the tip. The blade deformations at $Re_{tip} = 1.367 \times 10^6$ are shown in Fig. 9. The loading is consistent with the torsion added to the blade due to the structural deformations: the tip of the blade undergoes a torsion up to -0.8 degrees downwards. The trim state of each simulation is described in Tab. 2. The collective had to be increased for by about 0.5 degrees in the deformed cases

compared to the rigid ones to compensate for the blade torsion. The coning was also higher for the rigid blade simulations. The relatively high coning angle for the rigid blade may be due to the simplified aeromechanics algorithm used in the trimmer. The obtained torque coefficients are compared to Lorber *et al.*'s [18, 19] measurements in Fig. 10 and show good agreement. The predicted torque coefficients for deformed and undeformed blades are very close and these are mainly influenced by the Reynolds number. The structural deformation created some downward torsion at the tip of the blade, which had to be compensated by the increase of the collective. The influence of the structural deformation on the figure of merit is very limited (less than 1%), however, the figure of merit is always higher in the rigid case. This low influence was already noticed by Schmitz *et al.* [25]. However no more details about the differences between the rigid and elastic cases are detailed in this paper. The increase in the torque coefficient is mainly due to the changes in pressure ($C_{Q,P}$ part) rather than the viscous term.

The sectional thrust C_t is defined as $C_t = \frac{L_Z}{\frac{1}{2}\rho c V_{tip}^2}$, where L_Z is the loading in the vertical direction, and the sectional torque coefficient C_q as $C_q = \frac{L_M}{\frac{1}{2}\rho c^2 V_{tip}^2}$ where L_M is the moment around the rotating axis. The distribution of the sectional thrust and moments coefficients is compared with the experimental results of Lorber *et al.* [18, 19] in Fig. 11. On the main part of the blade, the obtained results are very close to the experiment, however the peak at the tip is over predicted. This poor prediction may be due to the approximations on the blade shape, due to uncertainties on the blade shape, or the location of the preceding blade tip vortex, which comes extremely close to the blade at about $r/R = 0.92$. The proximity of the preceding blade with the blade is clearly visible in Fig. 12. It passes just over the blade surface at about $r/R = 0.93$ and seems to have a strong influence on the air flow over the blade surface. However, the coning of the blade could not be compared to the experimental one, and neither is the position of the vortex from the preceding blade relatively to the blade position. A further study by Schmitz *et al.* [25] showed the effect of taking into account only the pressure at the tape locations and showed that the moment coefficient could be overestimated by more than 50% in the tip area. The influence of the Reynolds number showed only little effect, mainly at about $r/R = 0.90$ where the sectional lift and moment coefficient were slightly increased.

The pressure coefficients along the blade are plotted against the chord position and are shown in Fig. 13. The blade deformation increased the suction on the main part of the blade, but decreased it close to the tip, which is consistent with the torsional deformation undergone by the blade. The pressure coefficients from the simulations show good agreement with the experimental measurements up to the station at $r/R = 0.675$. The higher suction peak predicted on the elastic blade was closer to the experiment, particularly at $r/R = 0.40$. However, between $r/R = 0.775$ and $r/R = 0.92$, the suction peaks was under predicted and the pressure side showed a lower C_P . This explains the lower load in this part of the blade on the thrust distribution of Fig. 14. After $r/R = 0.945$, the suction on the upper surface is over predicted, explaining the higher predictions of the sectional thrust coefficient in the tip area in Fig. 11a. These re-

sults could be due to a poor interpretation of the local twist of the original blade, or the position of the vortex from the preceding blade, as explained previously. The predicted pressure coefficients show an equivalent angle of attack lower than the experimental predictions at the section $r/R = 0.865$ and higher at the sections $r/R = 0.945$ and $r/R = 0.965$. This is consistent with the vortex effect around $r/R = 0.92$ increasing the downwash at sections before $r/R = 0.92$ and decreasing it at sections after $r/R = 0.92$. The effect of the Reynolds number was limited on the pressure coefficients.

When the pressure coefficients are projected along the thickness of the aerofoil, as shown in Fig. 14, the differences between the simulation and experimental results appear clearer. This projection shows the effect of the pressure coefficient on the sectional torque of the rotor, and therefore the bigger the differences, the worse the prediction of the rotor torque. Due to the few measurement locations on the sections, some important features are not well captured, like the stagnation point. This lack of resolution can explain the important differences between the predicted and experimental sectional torque seen in Fig. 11b.

The vortex core location in the wake of the rotor has also been measured and compared to experimental results in Fig. 15. The effect of the Reynolds number on the vortex trajectories was marginal. The vortex vertical displacement is well predicted, while in the horizontal plane, the vortices tend to come slightly too fast inboard. Furthermore, after 270 degrees, the grid cells become too loose to accurately predict the location of the vortex cores and this explains the lack of agreement at the higher azimuth angles.

Overall, the flow predictions showed very good agreement with the experimental data on the main part of the blade. However the results showed discrepancies with experiments near the tip. These could be due to uncertainties in the blade definition or the influence of the preceding blade vortex. The lack of structural data for the model blade or the unknown blade shape during the experiment did not allow for a further investigation of this problem. The mesh deformation and trimming methods were found to be robust and needed a minimal increase of CPU cost.

3.3 HART-II Rotor in Forward Flight

The HART-II rotor was chosen to assess the effect of DES and mesh deformation on rotor flow predictions. Comprehensive experimental measurements were obtained by van der Wall *et al.* [31]. The rotor was tested in a slow descent flight, on a 6 degrees slope with an advance ratio $\mu = 0.1508$. The freestream Mach number is set at $M_\infty = 0.096$. The shaft angle is corrected for the wind-tunnel deviation and set to $\alpha_S = 4.5$ degrees. These conditions were chosen to test the prediction of blade-vortex interaction (BVI) events. The trim state was based on Lim *et al.*'s one [17] and was $\theta_0 = 3.36$ degrees, $\theta_{1c} = -1.57$ degrees and $\theta_{1s} = 0.97$ degrees. It was later found that an increase of θ_{1s} to $\theta_{1s} = 1.47$ (called *trimmed solution*) improved the results.

A first simulation was carried out on a grid with 17.6 million nodes, aiming at comparing the rigid and elastic blades. The blade deformation was extracted from the HART-II experiment database [30] and projected on the blade eigen-

modes obtained through NASTRAN, and the six first harmonics of each eigenmode amplitude during a revolution were extracted. This deformation was prescribed to the rotor blades. The obtained blade deformation at the tip is compared to experimental measurements in Fig. 16. The tip deformation matched well experimental measurements except the down peak in torsion at the front of the disk which is slightly under-predicted.

The main difference between the rigid one and elastic blade is visible in Fig. 17 which represents the evolution of the Mach-scaled normal coefficient along a revolution at $r/R = 0.875$. While the elastic blade was able to capture some BVI, the rigid one did not. On the other hand, the dissipation in the grid was too high and the vortices were too dissipated when interacting with the blade, which leads to the low amplitudes of the predicted BVI. Therefore, a new finer grid was generated and was also used to compare the SA and DES turbulence models for rotorcraft flows. The new grid size was set at 34.8 million nodes. The evolution of the Mach-scaled coefficient is also shown in Fig. 17. The new grid allowed for better capturing of the BVI events thanks to a lower grid dissipation. These are more numerous and have a higher amplitude, which is closer to experimental measurements. Further improvements are however necessary in terms of mesh density.

Isosurfaces of λ_2 criteria are shown in Fig. 18. The trajectory of the vortices is clearly shown: due to the descent pattern of the flight, the blade tip vortices are first convected over the rotor disk before going down because of the rotor downwash and crossing the rotor disk. This creates the BVIs and a high vortex resolution is needed to capture it without dissipating the vortices. Nevertheless, the combination of DES with structural deformation resulted in better overall results.

4 CONCLUSIONS

A CFD/CSD method has been developed and demonstrated for HMB. It includes a mesh deformation method and a rotor trimmer. The demonstration of the coupling strategy proved quick and efficient, requiring twice the CPU time compared to a rigid rotor computation in hover. The simulation of the UH-60A rotor showed limited differences between the rigid and elastic cases, but further investigation is necessary. A lack of comprehensive experimental database did not allow for further validation of the method.

The mesh deformation method was then used to prescribe the blade deformation on the HART-II rotor, and it allowed for capturing the BVI events for this case. A finer grid was, however, required to obtain a good resolution of the BVIs. This finer grid was also used to assess the differences between the SA and DES turbulence models. The comparison showed little difference, highlighting the need for extremely refined grids to allow the DES to capture more structures in the wake.

REFERENCES

- [1] P. Arcidiacono and R. Zincone. Titanium UTTAS Main Rotor Blade. *Journal of the American Helicopter Society*, 21(2):12–19, 1976.

- [2] A.R.M. Altmikus and S. Wagner and P. Beaumier and G. Servera. A Comparison: Weak versus Strong Modular Coupling For Trimmed Aeroelastic Rotor Simulations. American Helicopter Society 58th Annual Forum, June 2002.
- [3] O. Axelsson. *Iterative Solution Methods*. Cambridge University Press: Cambridge, MA, 1994.
- [4] P. Beaumier, E. Chelli, and K. Pahlke. Navier-Stokes Predictions of Helicopter Rotor Performance in Hover Including Aeroelastic Effects. *Journal of the American Helicopter Society*, 46(4):301–309, 2001.
- [5] R.T. Biedron and E.M. Lee-Rausch. Rotor Airloads Using Unstructured Meshes and Loose CFD/CSD Coupling. 26th AIAA Applied Aerodynamics Conference, Honolulu, HI, AIAA 2008-7341, August 18–21 2008.
- [6] F.J. Blom. Considerations on the Spring Analogy. *International Journal for Numerical Methods in Fluids*, 32:647–668, 2000.
- [7] A. Datta, J. Sitaraman, I. Chopra, and J.D. Baeder. CFD/CSD Prediction of Rotor Vibratory Loads in High-Speed Flight. *Journal of Aircraft*, 43(6):1698–1709, November–December 2006.
- [8] F. Dehaeze and G.N. Barakos. Hybrid Turbulence Models Evaluation for Rotorcraft Flows. 36th European Rotorcraft Forum, Paris, France, Paper 006, September 2010. .
- [9] L. Dubuc, F. Cantariti, M.A. Woodgate, B. Gribben, K.J. Badcock, and B.E. Richards. A Grid Deformation Technique for Unsteady Flow Computations. *International Journal for Numerical Methods in Fluids*, 32:285–311, 2000.
- [10] G.S.L. Goura, K.J. Badcock, M.A. Woodgate, and B.E. Richards. Implicit Method for the Time Marching Analysis of Flutter. *Aeronautical Journal*, 105(1046):199–214, April 2001.
- [11] D. Guenot. *Simulation des effets instationnaires a grande Ãlchelle dans les Ãlcoulements dÃlcollÃl's*. PhD thesis, SUPAERO, Toulouse, 2004.
- [12] H. Pomin and S. Wagner. Aeroelastic Analysis of Helicopter Rotor Blades on Deformable Chimera Grids. *Journal of Aircraft*, 41(3):577–584, May–June 2004.
- [13] K.S. Hamade and R.M. Kufeld. Modal Analysis of UH-60A Instrumented Rotor Blades. Technical Report TR-4239, NASA, 1990.
- [14] S.N. Jung, J.-S. Park, S.H. Park, and Y.H. Yu. Validation of HART II Structural Dynamics Predictions Based on Prescribed Airloads. American Helicopter Society Specialists' Conference on Aeromechanics, San Francisco, California, January 2010.
- [15] K. Pahlke and B.G. van der Wall. Chimera Simulations of Multibladed Rotors in High-Speed Forward Flight With Weak Fluid-Structure-Coupling. *Aerospace Science and Technology*, 9(5):379–389, July 2005.
- [16] K.C. Kim. Analytical Calculations of Helicopter Torque Coefficient (C_Q) and Thrust Coefficient (C_T) Values for the Helicopter Performance (HELPE) Model. Technical Report ARL-TR-1986, Army Research Laboratory, June 1999.
- [17] J.W. Lim and R.C. Strawn. Computational Modeling of HART II Blade-Vortex Interaction Loading and Wake System. *Journal of Aircraft*, 45:923–933, May–June 2008.
- [18] P.F. Lorber. Aerodynamic Results of a Pressure-Instrumented Model Rotor Test at the DNW. *Journal of the American Helicopter Society*, 36(4):12–19, October 1991.
- [19] P.F. Lorber, R.C. Stauter, and A.J. Landgrebe. A Comprehensive Hover Test of the Airloads and Airflow of an Extensively Instrumented Model Helicopter Rotor. 45th American Helicopter Society Forum, Boston, MA, May 22–24 1989. .
- [20] F.R. Menter. Two-Equation Eddy-Viscosity Turbulence Models for Engineering Applications. *AIAA Journal*, 32(8):1598–1605, 1994.
- [21] S. Osher and S. Chakravarthy. Upwind Schemes and Boundary Conditions with Applications to Euler Equations in General Geometries. *Journal of Computational Physics*, 50(3):447–481, June 1983.
- [22] M. Potsdam, H. Yeo, and W. Johnson. Rotor Airloads Prediction Using Loose Aerodynamic/Structural Coupling. *Journal of Aircraft*, 43(3):732–742, May–June 2006.
- [23] R. Steijl and G. Barakos and K. Badcock. A framework for CFD analysis of helicopter rotors in hover and forward flight. *International Journal for Numerical Methods in Fluids*, 51(8):819–847, 2006.
- [24] T. Rung, U. Bunge, M. Schatz, and F. Thiele. Restatement of the Spalart-Allmaras Eddy-Viscosity Model in Strain-Adaptative Formulation. *AIAA Journal*, 74(7):1396–1399, 2003.
- [25] S. Schmitz, M. Bhagwat, M.A. Moulton, F.X. Caradonna, and J.-J. Chattot. The Predictions and Validation of Hover Performance and Detailed Blade Loads. *Journal of the American Helicopter Society*, 54(1):1–12, 2009.
- [26] J. Sitaraman and B. Roget. Prediction of Helicopter Maneuver Loads Using a Fluid-Structure Analysis. *Journal of Aircraft*, 46(5):1770–1784, September–October 2009.
- [27] P. Spalart, W.H. Jou, M.Kh. Strelets, and S.R. Allmaras. Comments on the feasibility of LES for wings, and on a hybrid RANS/LES approach. In *Advances in DNS/LES*, Columbus, 1997.
- [28] P.R. Spalart and S.R. Allmaras. A One-Equation Turbulence Model for Aerodynamic Flows. *La Recherche Aérospatiale*, (1):5–21, 1994.

Coefficient	c_{b1}	σ	c_{b2}	κ	c_{w2}	c_{w3}	c_{v1}	c_{t1}	c_{t2}	c_{t3}	c_{t4}
Value	0.1355	2/3	0.622	0.41	0.3	2	7.1	1	2	1.1	2

Table 1: Closure coefficients for the SA model

- [29] K.E. Swalwell, J. Sheridan, and W.H. Melbourne. Frequency Analysis of Surface Pressures on an Airfoil After Stall. 21st Applied Aerodynamics Conference, Orlando, Florida, June 23–26 2003. .
- [30] B.G. van der Wall. Mode Identification and Data Synthesis of HART II Blade Deflection Data. Technical Report IB-111-2007/28, German Aerospace Center (DLR), 2007.
- [31] B.G. van der Wall, C.L. Burley, Y. Yu, H. Richard, K. Pengel, and P. Beaumier. The HART II test âĂŞ measurement of helicopter rotor wakes. *Aerospace Science and Technology*, 8(4):273–284, June 2004.

Case	Reynolds number	θ_0	β_0	C_T	$C_{Q,P}$	C_Q	FM
Inviscid - Rigid blade	—	8.07	4.74	0.01374	0.001015	0.001015	0.7936
Viscous - Rigid blade	1.367×10^6	8.42	5.48	0.01403	0.001017	0.001083	0.7231
Viscous - Elastic blade	1.367×10^6	8.94	4.21	0.01406	0.001023	0.001157	0.7206
Viscous - Rigid blade	7.833×10^6	8.23	5.07	0.01402	0.000982	0.001070	0.7758
Viscous - Elastic blade	7.833×10^6	8.71	4.21	0.01403	0.000983	0.001072	0.7746

Table 2: Trim state and integrated coefficients for the various UH-60A calculations.

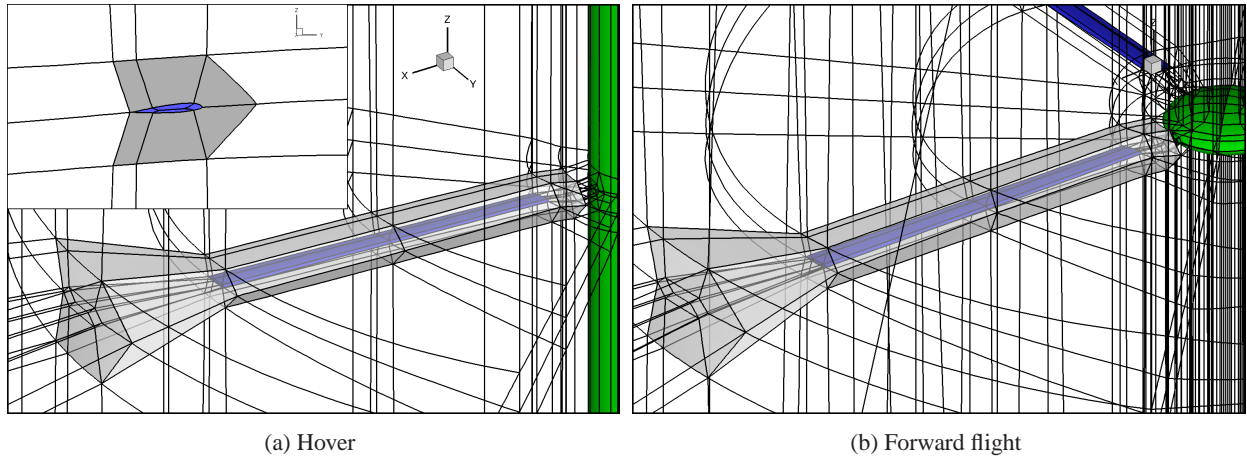


Figure 1: Multi-block grid topology used for HMB in hover and forward flight, showing the blade (blue), the cylindrical hub (green) and the rigid blocks (translucent grey). A section perpendicular to the blade span at the tip is shown in the upper left corner.

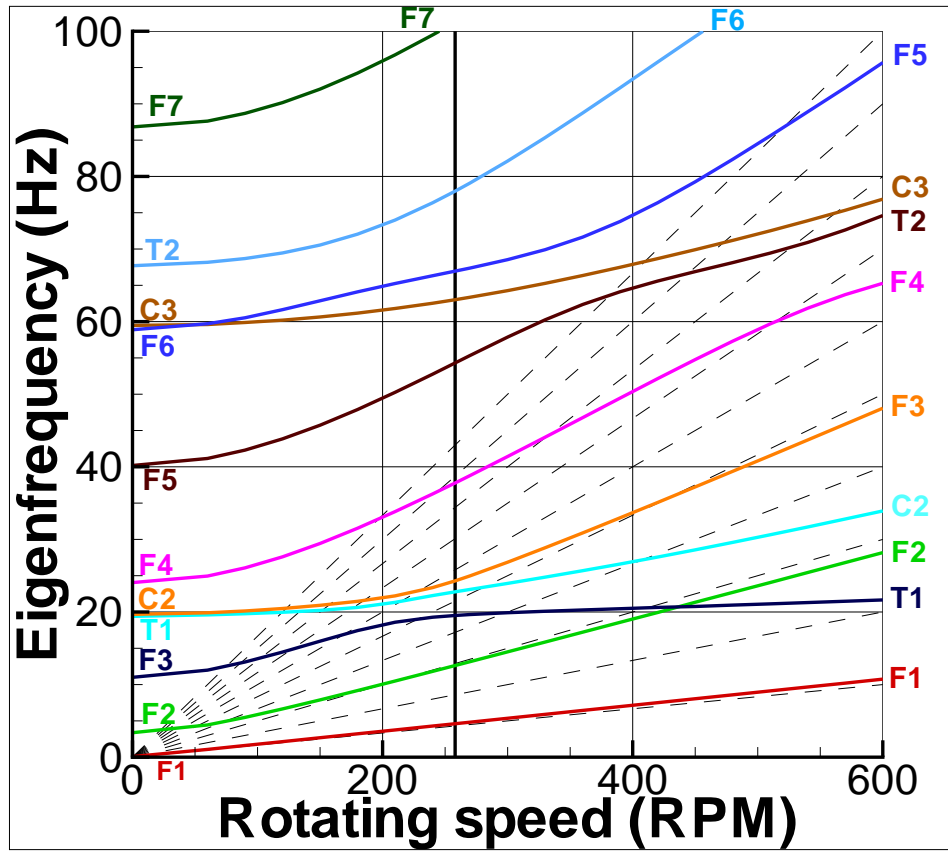


Figure 2: Evolution of the UH-60A blade eigenfrequencies with the rotational speed.

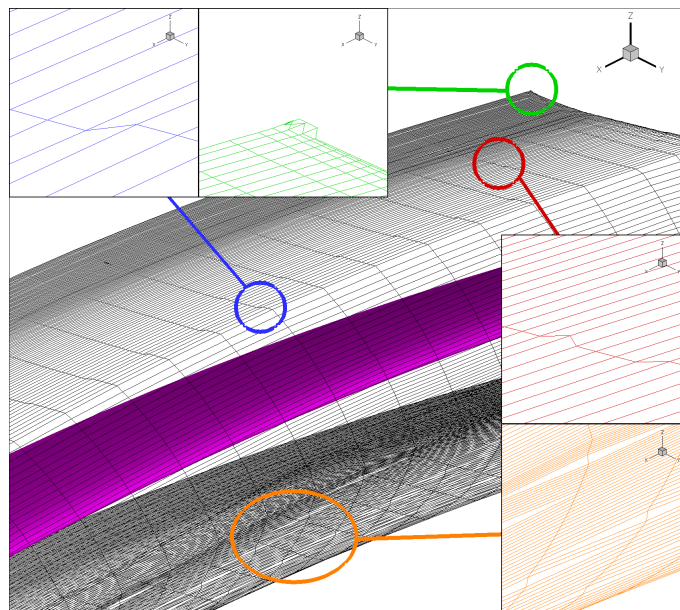


Figure 3: Distortion of the mesh due to the use of CVT far from the blade surface.

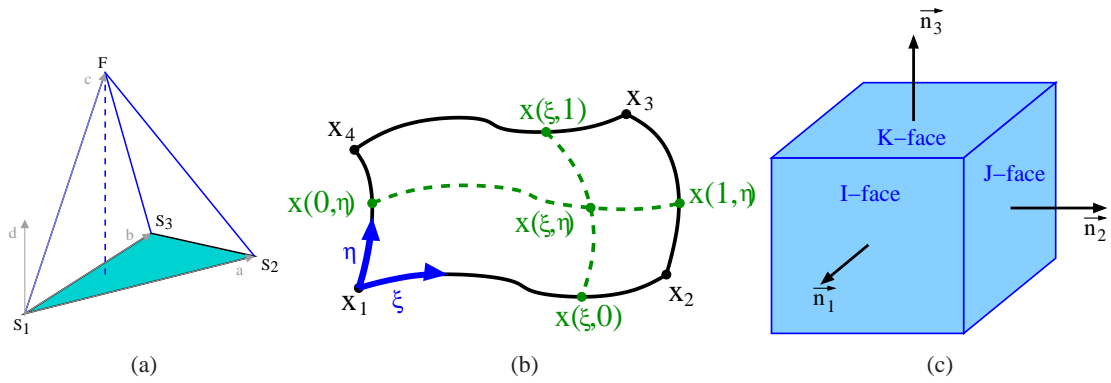


Figure 4: (a) Notations for the association of a fluid node F with a triangular element (S_1, S_2, S_3) using CVT. (b) Notation for the TFI application on a block face. (c) Notation for cell skewness definition.

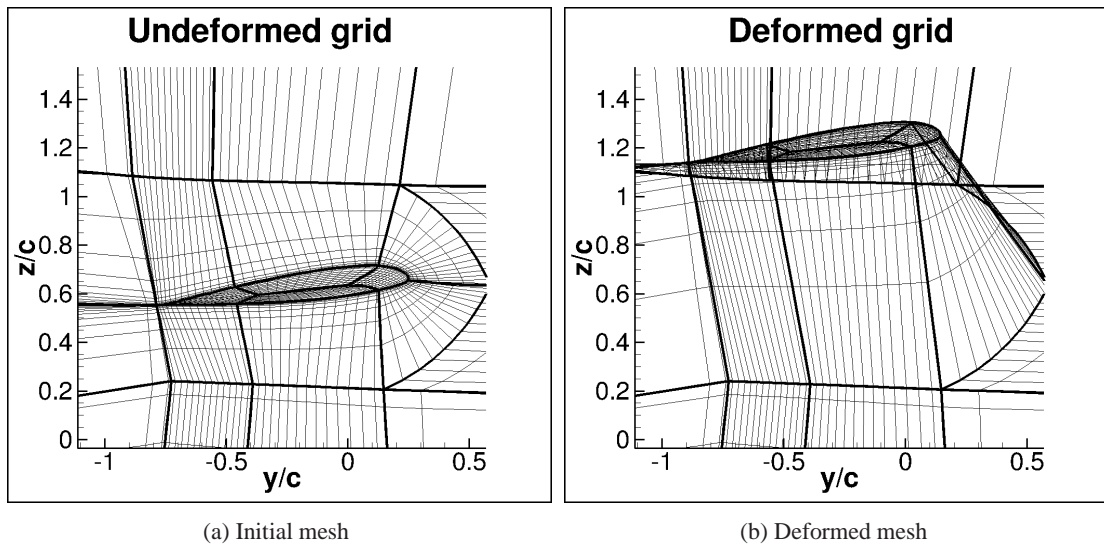


Figure 5: Limitations on the displacement amplitude due to the use of CVT and TFI. The blade tip was moved vertically with an amplitude of $0.6c$ outside the C-part of the mesh.

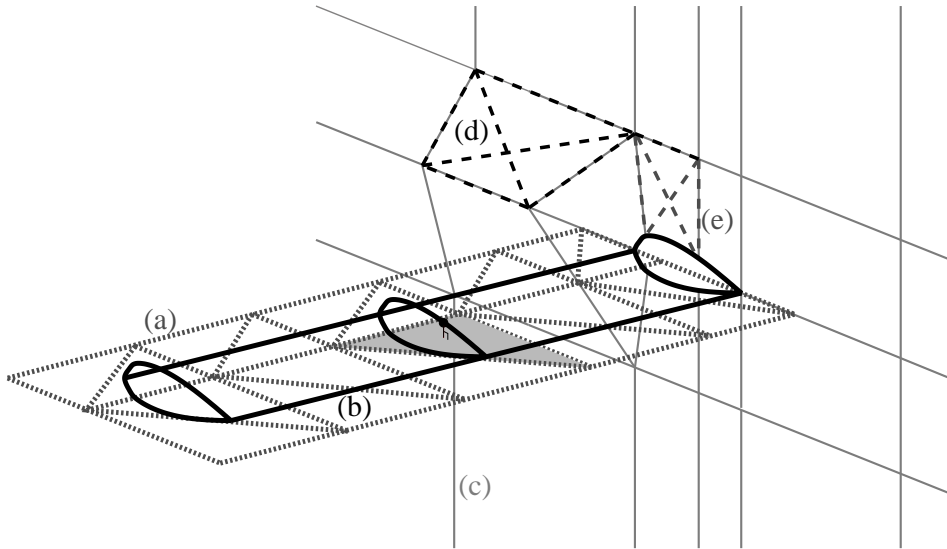


Figure 6: Projection of the fluid grid on the structural model through CVT. The blade structural model (a) is in grey short dashed line and the projection element in light grey. The blade shape (b) is represented in black. The fluid mesh block boundaries are shown in light grey (c), and the springs created for the spring analogy are shown in two block faces: in grey long dashed lines when in contact of the blade (e) and black long dashed lines otherwise (d).

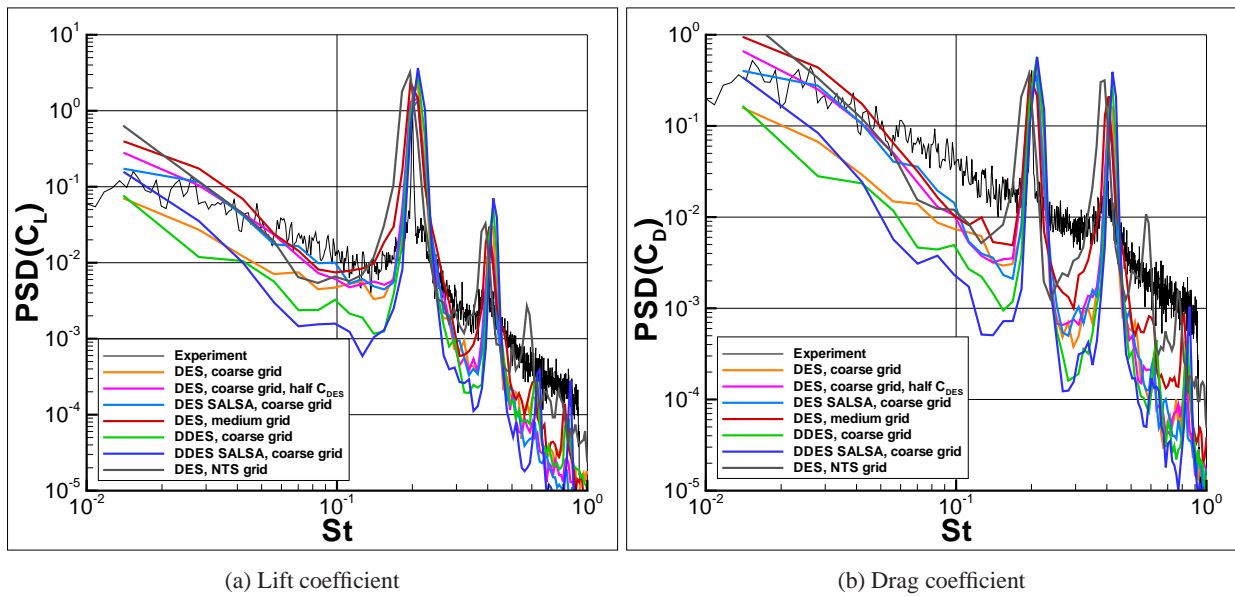


Figure 7: Spectra of lift and drag coefficients of a NACA0021 aerofoil at 60 degrees incidence obtained with various turbulence models on the coarse and fine grids.

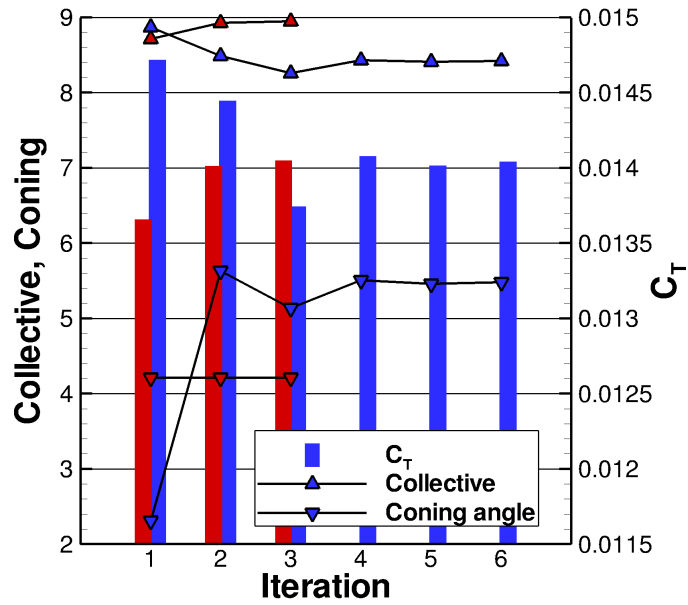


Figure 8: Trimming convergence history of the UH-60A rigid (blue) and elastic (third iteration, red) blades in hover during viscous calculations at $Re_{tip} = 1.367 \times 10^6$.

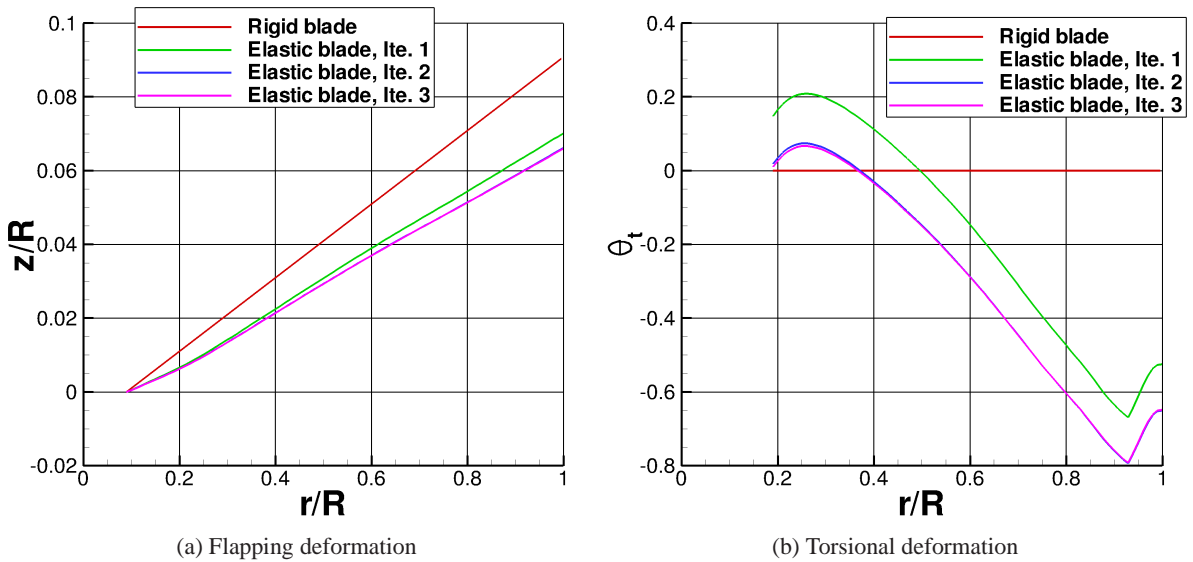


Figure 9: UH-60A blade deformation obtained from viscous calculations at $C_T/\sigma = 0.170$ at $Re_{tip} = 1.367 \times 10^6$, taken at the quarter chord line.

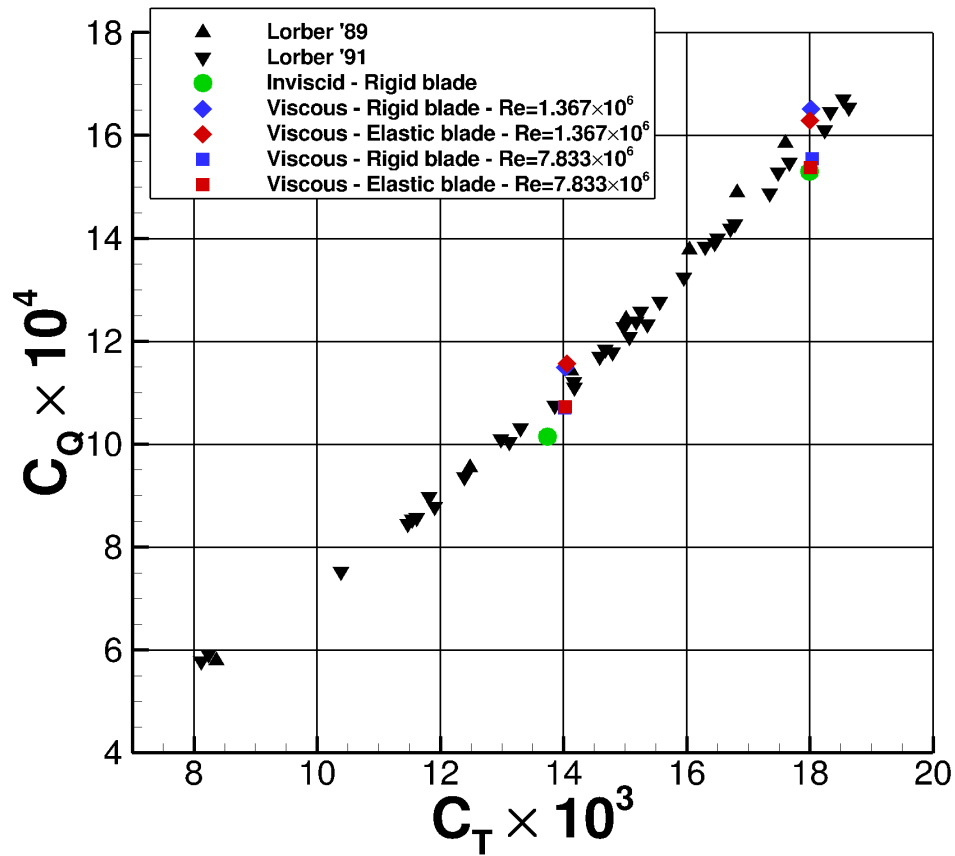


Figure 10: Comparison of the thrust and torque coefficients (C_T and C_Q respectively) with experimental measurements from Lorber *et al.* [18, 19].

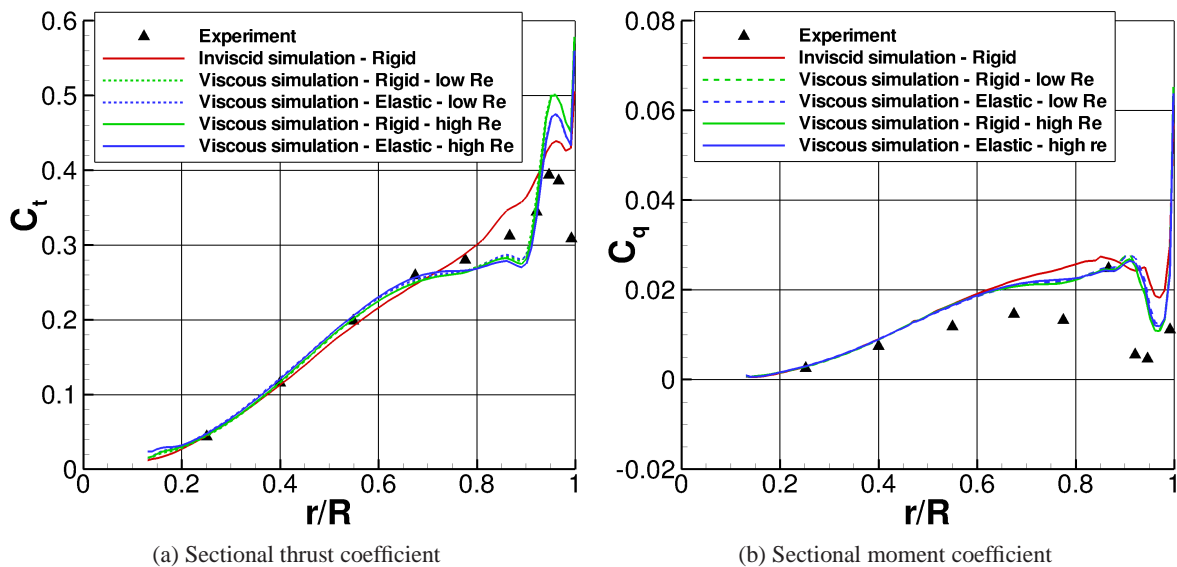


Figure 11: Comparison of the computed sectional thrust and moment coefficients (C_t and C_q respectively) along the rotor radius with the experiments from Lorber *et al.* [18, 19].

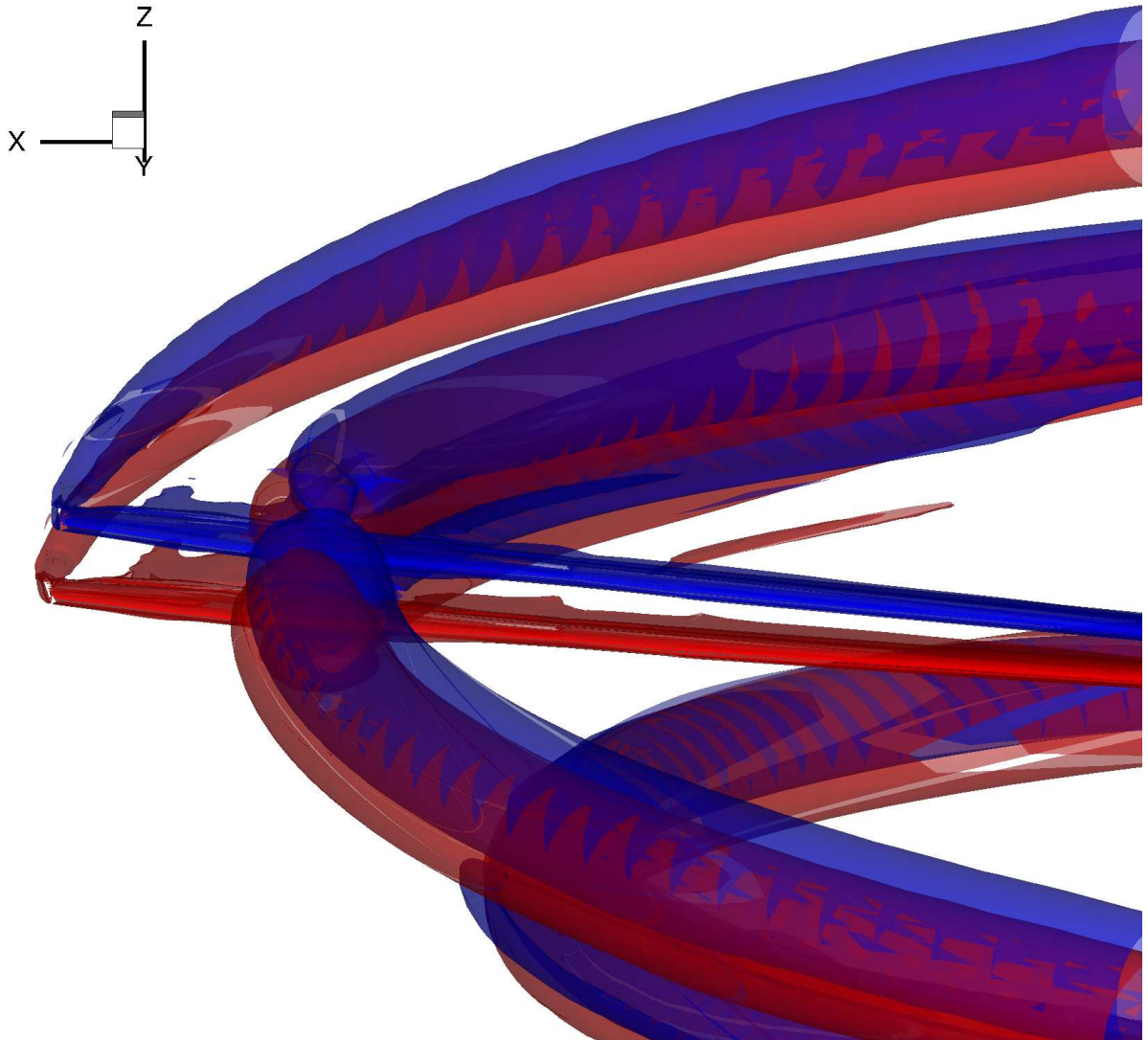


Figure 12: Wake visualisation in the tip area of hovering undeformed (blue) and undeformed (red) UH-60A full-scale rotors at $C_T/\sigma = 0.170$.

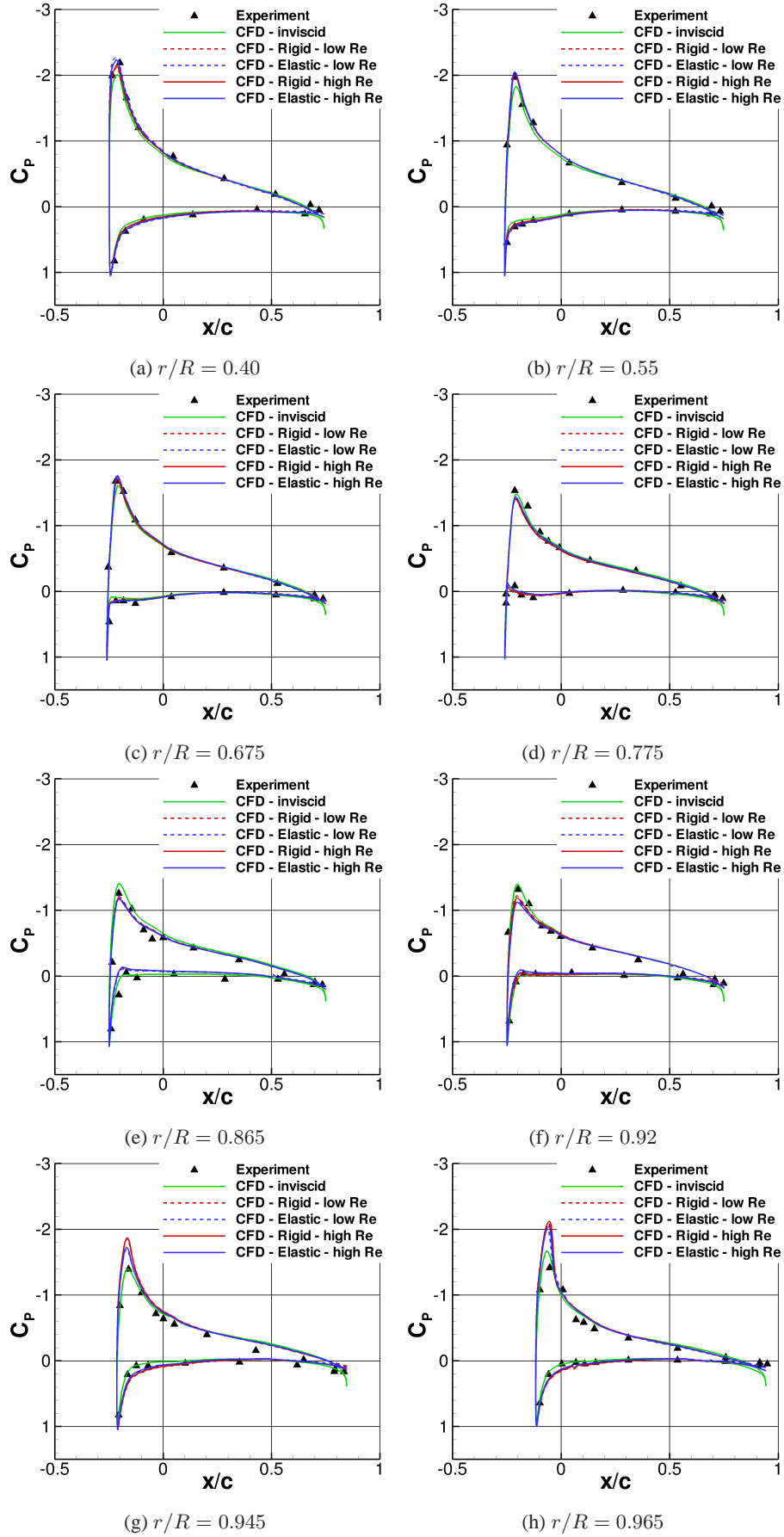


Figure 13: Comparison of the sectional pressure coefficients at various blade radial positions obtained with a rigid and elastic blade simulation with experimental measurements for hovering model (low Re) and full-scale (high Re) UH-60A rotors at $C_T/\sigma = 0.170$. Experiments by Lorber *et al.* [19]

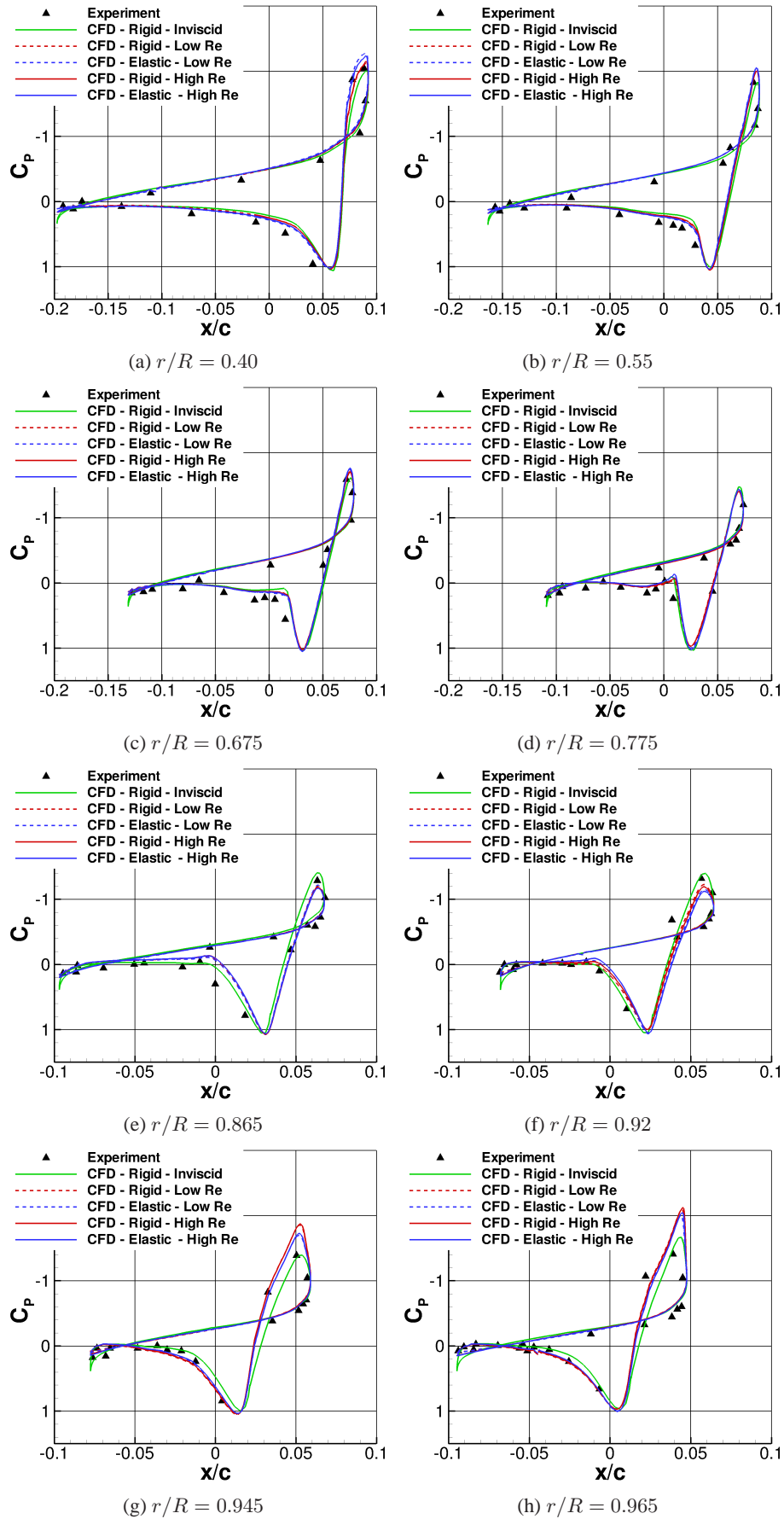


Figure 14: Comparison of the sectional pressure coefficients at various blade radial positions obtained with a rigid and elastic blade simulation with experimental measurements for hovering model (low Re) and full-scale (high Re) UH-60A rotors at $C_T/\sigma = 0.170$. The pressure coefficients are projected on the aerofoil thickness. Experiments by Lorber *et al.* [19]

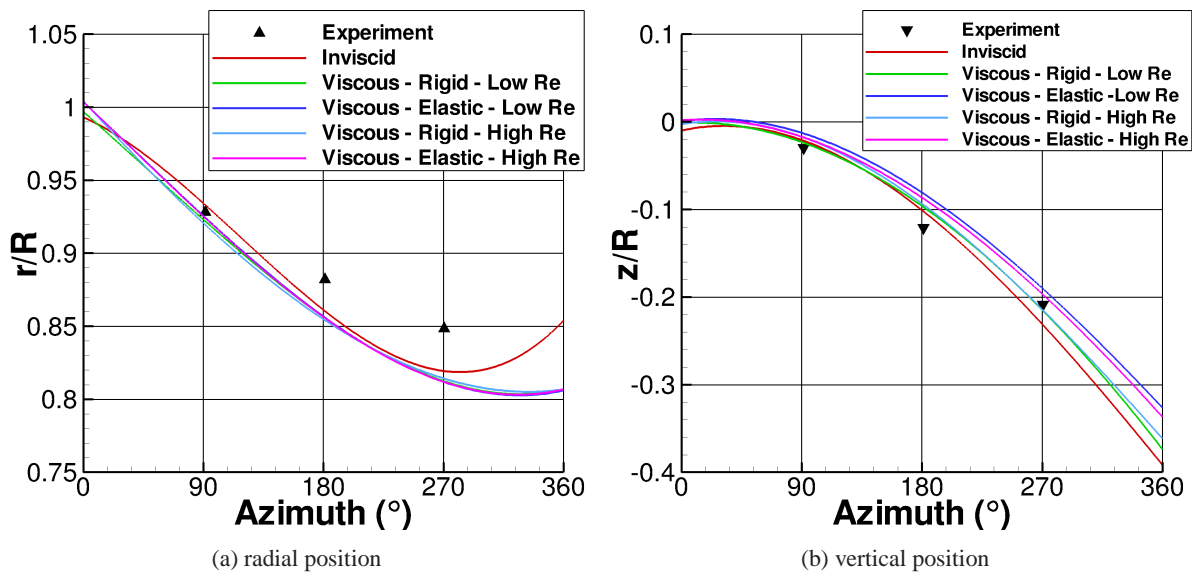


Figure 15: Vortex radial and vertical location in the wake of hovering UH-60A model (low Re) and full-scale (high Re) rotors at $C_T/\sigma = 0.170$. Experiments by Lorber *et al.* [19]

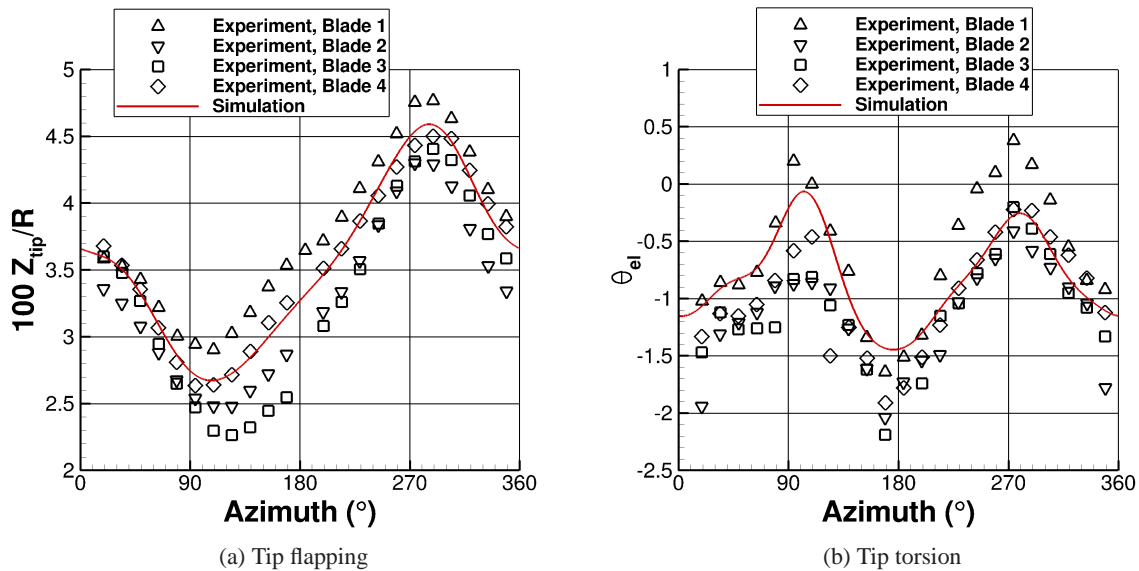


Figure 16: HART-II rotor blade deformation used in the CFD simulation compared to experimental measurements at the blade tip. Experiments by van der Wall *et al.* [31].

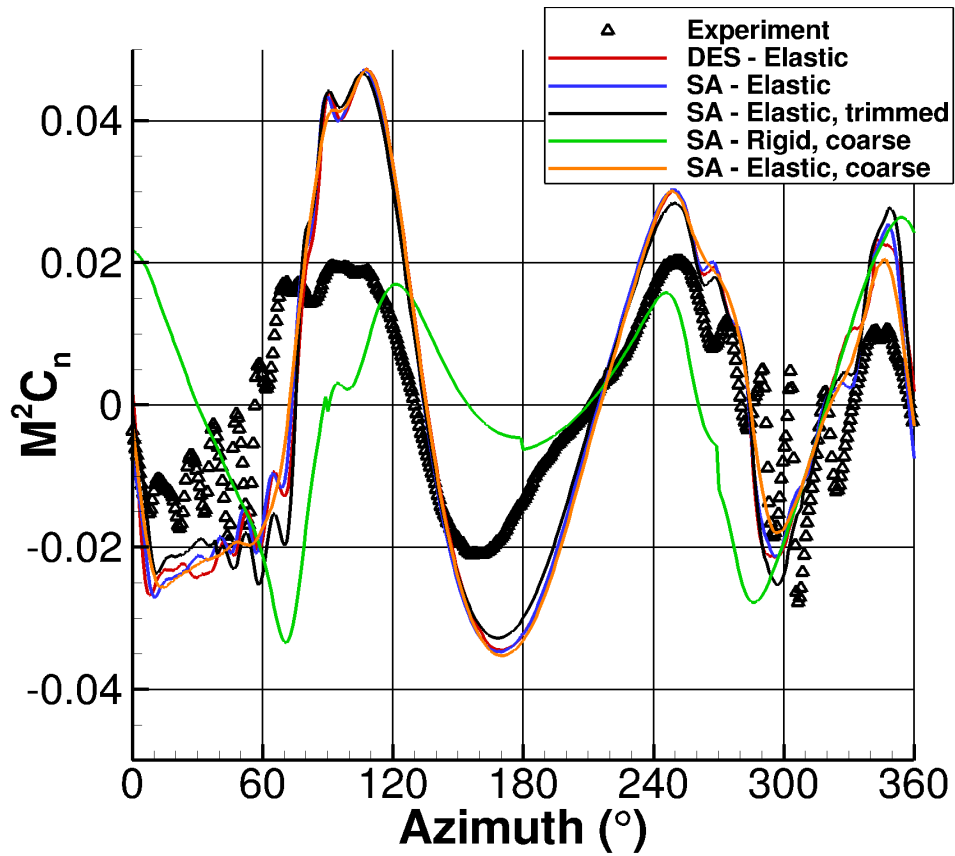


Figure 17: Comparison of the Mach-scaled coefficient at $r/R = 0.875$ during a revolution of the HART-II rotor with experimental measurements, mean and first harmonics removed. Experiments by van der Wall *et al.* [31].

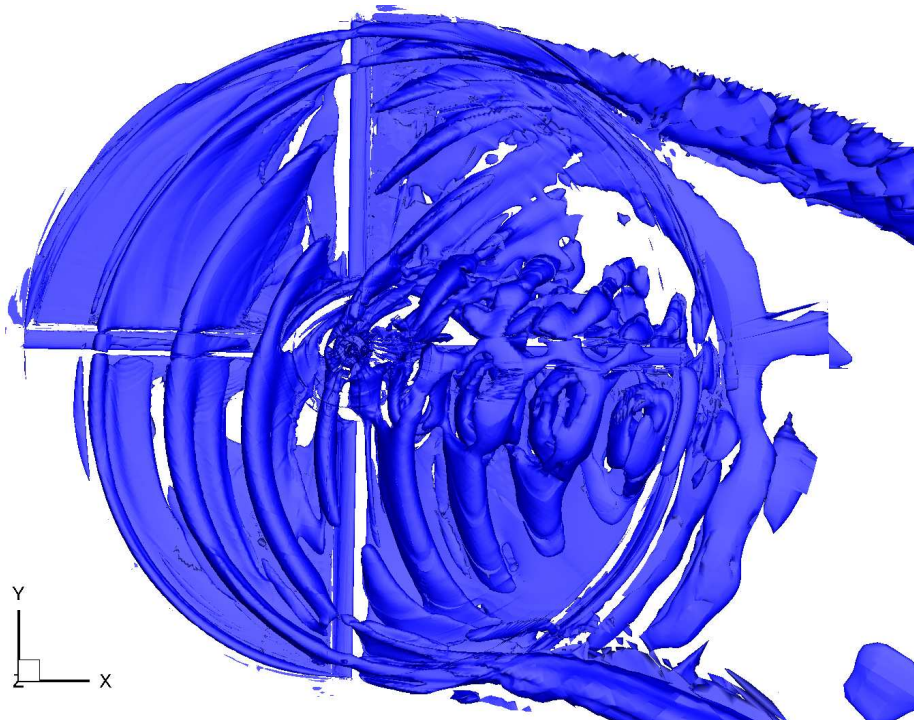


Figure 18: Isosurface of λ_2 criterion in the HART-II test case.